SCIENCE CHINA Materials

ARTICLES

mater.scichina.com link.springer.com

Published online 7 August 2017 | doi: 10.1007/s40843-017-9074-x
*Sci China Mater* 2017, 60(8): 755–765

# *In-situ* phase transition to form porous h-$MoO_3$@C nanofibers with high stability for $Li^+$/$Na^+$ storage

Zhi Chen[1†], Yongkang Liu[1†], Hang Zhang[2], Shuangshuang Ding[1], Taihong Wang[1] and Ming Zhang[1*]

**ABSTRACT** **Porous h-$MoO_3$@C nanofibers with a large specific surface area of 400.2 $m^2$ $g^{-1}$ were successfully synthesized with hot $HNO_3$ oxidizing $MoO_2$@C nanofibers without obvious damage to carbon shells. As anodes for lithium ion batteries (LIBs), the porous h-$MoO_3$@C nanofibers electrodes show a reversible capacity of 302.9 mA h $g^{-1}$ at 2 A $g^{-1}$ after 500 cycles. As anodes for sodium ion batteries (SIBs), they also can deliver a good rate capacity and hold 108.9 mA h $g^{-1}$ at 2 A $g^{-1}$ after 500 cycles, even can have 91 mA h $g^{-1}$ at 5 A $g^{-1}$ after 1200 cycles. The excellent electrochemical performances of the porous h-$MoO_3$@C nanofibers are attributed to the unique structure which not only can maintain the structure stability but also provide enough active sites for $Li^+$/$Na^+$. At the same time, the tunnel structure of h-$MoO_3$ can lead to separate electron–hole and offer a great deal of special positions for cation ($Li^+$/$Na^+$) insertion/extraction. The present method may be helpful for the synthesis of transition metal oxides (TMOs)-carbon composites with high valence metal atoms in the field of batteries and catalysts.**

**Keywords:** electrospinning, *in-situ* phase transition, lithium ion battery, sodium ion battery, core shell nanofibers

## INTRODUCTION

Lithium ion batteries (LIBs) have received wide attention in the commercial market of portable electronic devices [1,2], energy storage systems [3–4], and electric vehicles [5–6] due to their excellent characteristics, such as long cycling life, high energy density, and no memory effect [7–9]. However, with the rapid development of science and technology, the researches of higher capacity and longer cycling performance of LIBs have become urgent. On the other hand, sodium ion batteries (SIBs) have recently received wide publicity as an energy storage system due to more natural abundance of Na reserves [10,11]. The theoretical capacity of the traditional commercial graphite anode is only 372 mA h $g^{-1}$ for LIBs [12,13], even lower for SIBs [14,15], limiting the application of high efficiency energy demand with high stability both for LIBs and SIBs. Thus, it has been drawing wide attention to develop new anode materials, which not only have relatively high capacity but also maintain good cycling stability.

In recent years, transition metal oxides (TMOs) in optics [16,17], magnetism [18,19], catalysis [20,21] and electronic fields [22,23] show superior performance, and the nano-sized TMOs have been used as anode materials for LIBs, and considered as promising candidates to solve the above mentioned problems [24–28]. Compared to graphite anodes, they have high theoretical capacity, such as $MoO_3$ (1,117 mA h $g^{-1}$) [29,30], including the well-known thermodynamically stable normal phase α-$MoO_3$ [31,32], and metastable phase h-$MoO_3$ [33,34]. As reported, metastable structures often demonstrate new or enhanced properties compared to their thermodynamically stable forms. For example, the tunnel structure of h-$MoO_3$ can lead to separate electron hole and offer a great deal of special positions for the cation ($Li^+$/$Na^+$) insertion/extraction [35]. And the electrical conductivity of h-$MoO_3$ is better than that of the stable phase α-$MoO_3$ [36]. However, h-$MoO_3$ still faces the risk of volume expansion, leading to poor kinetics and capacity decrease during the charge/discharge process [37].

So the urgent issue is how to enhance the stability of the structure. Carbon composite structures have been widely studied, such as core shell structure [38–40], which is considered as an effective structure to solve the above problems. For instance, Xia *et al.* [41] synthesized $MoO_3$/C nano-composites with a capacity of about 500 mA h $g^{-1}$ at

[1] Key Laboratory for Micro-Nano Optoelectronic Devices of Ministry of Education, School of Physics and Electronics, Hunan University, Changsha 410082, China
[2] College of Chemistry and Chemical Engineering, Hunan University, Changsha 410082, China
[†] These authors contributed equally to this work.
[*] Corresponding author (email: zhangming@hnu.edu.cn)

the 100th cycle at a current density of 0.1 A $g^{-1}$ for LIBs. Pan's group [42] have prepared $MoO_3$/reduced graphene oxide delivering a capacity of about 208 mA h $g^{-1}$ at 0.05 A $g^{-1}$ after 50 cycles for SIBs. Hence, the shell, such as carbon or graphene, is the key factor to improve the stability and electroconductivity of the structure, which further affects the performance of the batteries. More importantly, according to previous studies [43–45], the existence of porous structure can improve the electrochemical performance of carbon materials, boosting the electron transfer at the electrode/electrolyte interface and reducing the structural collapse caused by the volume change. Herein, porous h-$MoO_3$@C nanofibers have been successfully synthesized with hot $HNO_3$ oxidizing $MoO_2$@C nanofibers, which are prepared by a single electrospinning. On the one hand, $MoO_3$ has a higher theoretical specific capacity than $MoO_2$. On the other hand, some of $MoO_2$ nanoparticles in the nanofibers are dissolved by hot $HNO_3$, and the rest coated by carbon undergo *in-situ* phase transition and then are oxidized to form porous h-$MoO_3$@C nanofibers. So the porous nanofiber structures not only provide free space for volume expansion, but also facilitate the migration of $Li^+$/$Na^+$. At the same time, the surface modification (–OH, C=O, C–$NO_2$, –$NH_2$) by hot $HNO_3$ on the surface of the porous h-$MoO_3$@C nanofibers can further enhance the cyclic stability. As anodes for LIBs and SIBs, the porous h-$MoO_3$@C nanofiber electrode shows excellent performance. This strategy provides a new route to synthetize core shell nanomaterials, which are both for LIBs and SIBs.

## EXPERIMENTAL SECTION

### Synthesis of $MoO_2$@C nanofibers

The mixture of ammonium molybdate tetrahydrate (AMM, $(NH_4)_6Mo_7O_{24}{\cdot}4H_2O$, 99%) and polyvinyl alcohol (PVA, $[C_2H_4O]_n$, $M_w$=80,000, 1 g) were dissolved in deionized water (10 g) at 60°C with continuous stirring for 8 h, which formed a mixed solution of a viscous gel. The distance between the tip of the spinneret and the collector was adjusted to 16 cm. The voltage and the speed were 17 kV and 0.4 mL $h^{-1}$, respectively. The as-prepared precursors in vacuum were dried at 80°C overnight, and then heated at 650°C for 2 h at a rate of 1°C $min^{-1}$ in Ar to obtain $MoO_2$@C nanofibers. The pure $MoO_3$ was obtained by annealing AMM at 650°C for 2 h in air.

### Synthesis of porous h-$MoO_3$@C nanofibers

The $MoO_2$@C nanofibers (0.1 g) were added to the mixed solution of deionized water (60 ml) and concentrated nitric acid (5 mL, about 14.4 mol $L^{-1}$) at 80°C for 20 h. Finally h-$MoO_3$@C nanofibers were obtained by centrifugation several times, and then dried at 60°C.

### Characterization

The samples were characterized by X-ray diffraction (XRD Cu Kα irradiation, $\lambda$=1.5418 Å), scanning electron microscopy (SEM, Hitachi S4800), transmission electron microscopy (TEM, JEOL-2010), X-ray photoelectron spectroscopy (XPS), Brunauer-Emmett-Teller (BET), Fourier-transform infrared (FTIR, AVTA-TAR, 370), X-ray photoelectron spectroscopy (XPS) and thermogravimetric analysis (TGA).

### Electrochemical measurements

The electrochemical performance was tested using CR2025-type coin cells. The active materials (70 wt.%), conductivity agent carbon black (15 wt.%) and binder sodium carboxymethyl cellulose (CMC, 15 wt.%) were mixed in deionized water and absolute alcohol mixture by stirring at a constant speed for 8 h, and a homogeneous slurry was obtained, which acted as the electrode materials. The mixed slurry was then spread onto a copper foil and dried at 80°C in a vacuum oven for 12 h. The electrolyte contained a solution of 1 mol $L^{-1}$ $LiPF_6$ in diethyl carbonate/ethylene carbonate/dimethyl carbonate (1:1:1, in wt./wt.). These cells were assembled in an argon filled glovebox ($O_2$ and $H_2O$ levels less than 0.05 ppm). The charge/discharge capacities were calculated based on the composite active materials (h-$MoO_3$@C nanofibers or $MoO_2$@C nanofibers). Cyclic voltammetry (CV) curves were tested using Chen Hua CHI 660E electrochemical station. The charge discharge measurements were carried out on an Arbin BT2000 system with the potential window of 0–3 V.

## RESULTS AND DISCUSSION

The synthesis of porous h-$MoO_3$@C nanofibers is briefly outlined in the schematic diagram, as shown in Fig. 1a. First of all, AMM/PVA precursor was prepared by electrospinning. After annealing at 650°C in Ar, the $MoO_2$@C nanofibers were synthesized. Then after the hot $HNO_3$ treatment, some of $MoO_2$ nanoparticles in the nanofibers were dissolved and others coated by carbon were oxidized by *in-situ* phase transition, forming a porous structure of $MoO_3$@C nanofibers. At the same time, some oxygen-containing functional groups were modified on the surface of the $MoO_3$@C nanofibers. The crystal structures of $MoO_2$ and h-$MoO_3$ are provided, as shown in Fig. 1b, which more vividly elaborates the transition from $MoO_2$ to

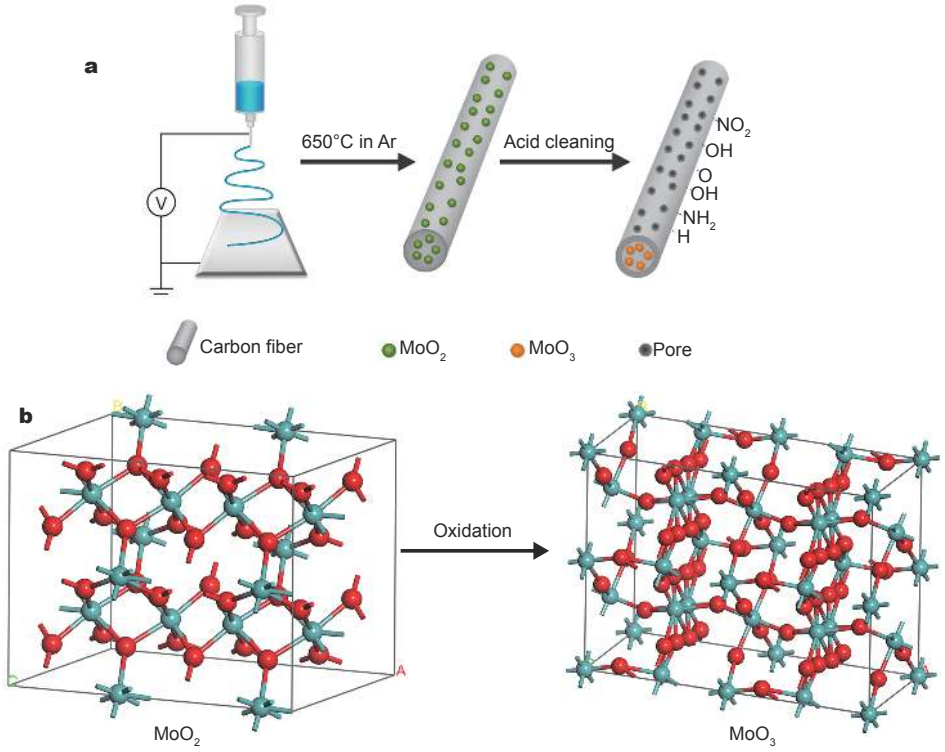


**Figure 1** (a) Schematic illustration shows the synthetic route for preparing porous h-$MoO_3$@C nanofibers; (b) the transition of crystal structure from $MoO_2$ to $MoO_3$ through hot $HNO_3$ oxidation.

h-$MoO_3$.

The micro morphologies of the as-synthesized products were analyzed by SEM. The image of the $MoO_2$@C nanofibers after annealing at 650°C with a rate of 1°C $min^{-1}$ in Ar is shown in Fig. 2a, which clearly reveals the core shell structures. The XRD diffractions can be readily indexed to $MoO_2$, which shows that the AMM is absolutely converted to $MoO_2$, as shown in Fig. 2c. The content of $MoO_2$ in the $MoO_2$@C nanofibers is 63% in Fig. S1 (Supplementary information) by TGA. After acid treatment, the XRD of the product is shown in Fig. 2d, and all the identified peaks can be indexed to h-$MoO_3$ (JCPDS No. 21-569), which is due to the oxidation of $MoO_2$, but the content of $MoO_3$ becomes only 26.24 % in Fig. S1, the reason for which is that some of the $MoO_2$ nanoparticles were dissolved in $HNO_3$ solution and the rest underwent phase transition and then were oxidized to form h-$MoO_3$@C nanofibers. So in Fig. 2b, the core shell structure still exists and the surface of nanofibers becomes slightly rough with lots of pores. At the same time more SEM images of $MoO_2$@C and h-$MoO_3$@C nanofibers are shown in Fig. S2. The reasons for the formation of core shell structure were explained in our previous reports [46,47].

In order to further distinguish the micro structures of the $MoO_2$@C and h-$MoO_3$@C nanofibers, TEM was characterized. In Fig. S3, the image of the $MoO_2$@C nanofibers clearly indicates that $MoO_2$ nanoparticles are coated by carbon. After acid treatment, the TEM image of the h-$MoO_3$@C nanofibers is shown in Fig. 3a with a porous structure. Fig. 3b confirms the presence of crystalline h-$MoO_3$ coated by carbon with a characteristic plane of (410). The $N_2$ adsorption-desorption isotherms of the h-$MoO_3$@C nanofibers exhibit type-IV isotherm associated with a surface area of 400.2 $m^2$ $g^{-1}$. The inset in Fig. 3c shows that the pore-size of nanofibers is micropores and mesopores. The porous nanostructure would provide more favorable transportation route, while the high surface area affords more adsorption sites for $Li^+$/$Na^+$, serving as reservoirs for $Li^+$/$Na^+$ storage and channels for easy permeation of electrolyte [47]. At the same time, the oxygen-containing functional groups are also characterized by FTIR shown in Fig. 2d. With hot $HNO_3$ treatment, the surface of the h-$MoO_3$@C nanofibers are modified with oxygen-containing functional groups (–OH, –C=O), which can form stable solid electrolyte interface (SEI) films, further enhancing the cyclic stability [48].

In Fig. 4a, the porous h-$MoO_3$@C nanofibers were composed solely of C, O, N and Mo. The corresponding O

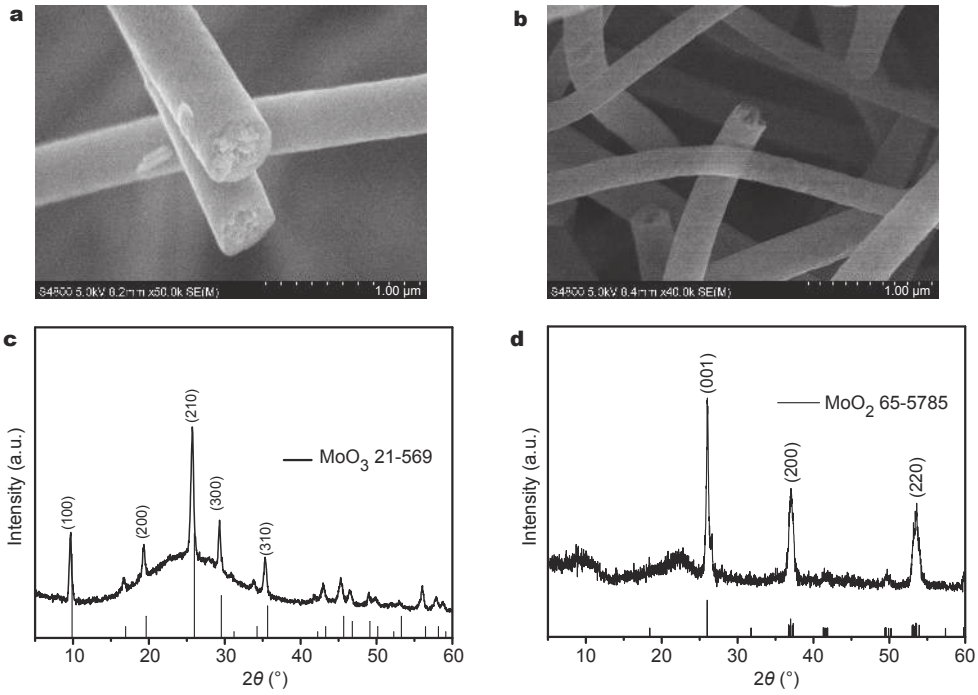


**Figure 2** (a, b) SEM images of the as-synthesized $MoO_2$@C and h-$MoO_3$@C nanofibers, respectively; (c, d) XRD of the $MoO_2$@C and h-$MoO_3$@C nanofibers, respectively.

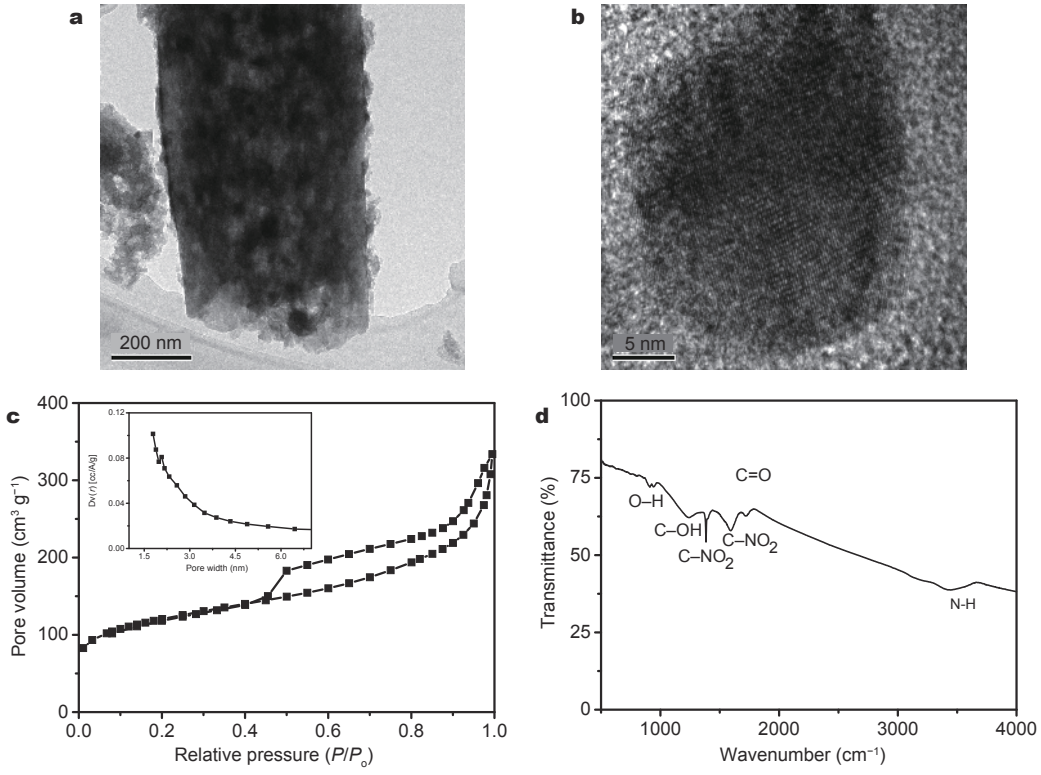


**Figure 3** (a, b) TEM images of the h-$MoO_3$@C nanofibers; (c) nitrogen adsorption/desorption isotherms of the h-$MoO_3$@C nanofibers (the inset is the pore-size distribution); (d) FTIR spectrum of the h-$MoO_3$@C nanofibers.

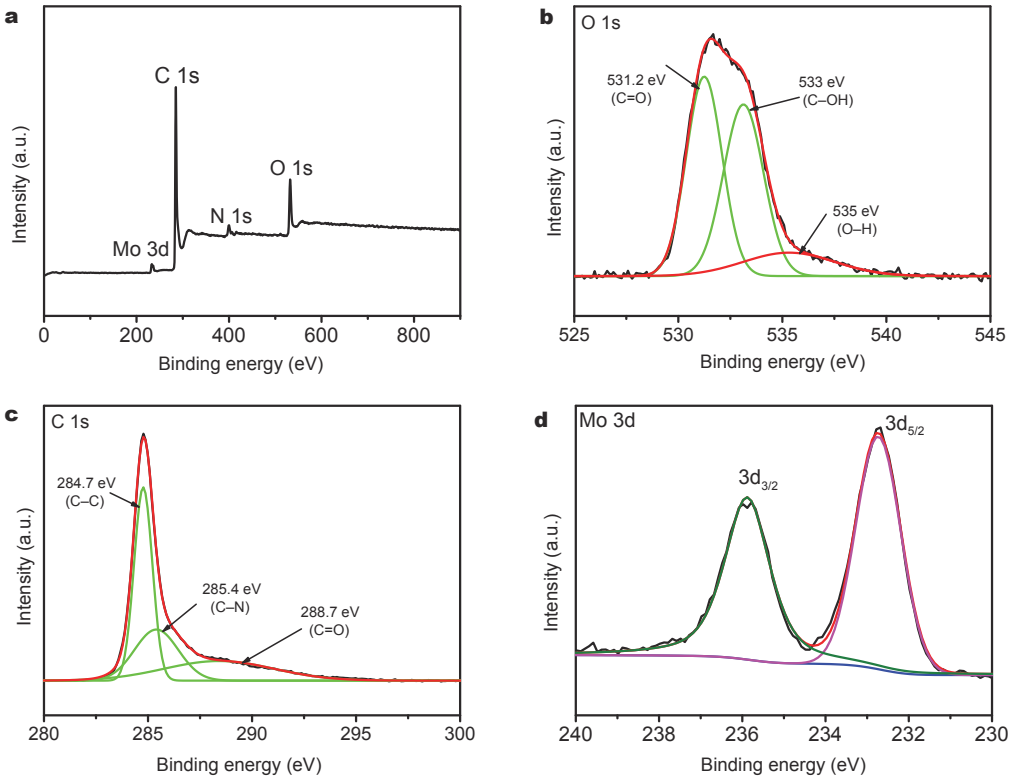


**Figure 4** Low-resolution XPS spectrum (a), high-resolution XPS spectra of (b) C 1s, (c) O 1s, and (d) Mo 3d of the h-$MoO_3$@C nanofibers.

1s spectra (Fig. 4b) exhibits signals corresponding to C=O and C–OH at ≈ 531.2 and 533 eV, respectively. The peak at 535 eV is a fingerprint of OH groups. The result well proved that oxygen-containing functional groups are modified on the surface of nanofibers in line with the FTIR result. Furthermore, the high-resolution C 1s spectra (Fig. 4c) exhibits a main peak corresponding to C–C at 284.7 eV, along with a single one for C–N at 285.4 eV, and a further weaker band associated with C=O at 288.7 eV. Fig. 4d shows the two peaks at 235.8 and 232.7 eV are attributed to the binding energies of the $3d_{3/2}$ and the $3d_{5/2}$ orbital electrons of $Mo^{6+}$ [29], respectively, indicating that there is no existence of $Mo^{4+}$.

The samples during charge/discharge process are tested by CV over the voltage range of 0–3.0 V at the scanning rate of 0.1 mV $s^{-1}$ for LIBs, as shown in Fig. 5a. The peak at 2.02 V is only observed in the first discharge cycle, which comes from a solid SEI layer and the decomposition of the electrolyte [49–51]. In the subsequent CV steps, the main oxidation/reduction pair is 1.2/1.46 V, associating with the reaction of $MoO_3$ [52,53]. The peaks (0.42 V) may be from $Li_xMo$ alloys, which is due to the $Li^+$ insertion/extraction with different site energies for different nanostructures and composites [53]. The broad peak at 2.5 V should be due to the desertion of $Li^+$ from crystalline $Li_xMoO_3$ [29]. The oxidation peaks near 0 V are attributed to the carbon, which is more obvious and shows the electrode possesses good electrochemical performance in the process of charge/discharge [46].

Fig. 5b shows the charge/discharge curves for the h-$MoO_3$@C nanofiber electrode at the current density of 0.1 A $g^{-1}$ over the voltage range of 0–3.0 V. It was observed in the first cycle that the charge and discharge capacity of the h-$MoO_3$@C nanofiber electrode can reach 878.1 and 1,595.3 mA h $g^{-1}$, respectively, which may be caused by activation. And the Coulombic efficiency is estimated as 55%, which is caused by the formation of SEI and the decomposition of the electrolyte [54,55]. In the next cycles, the Coulombic efficiency of the electrode could reach 99%.

As illustrated in Fig. 5c, the rate performances were tested at the current densities of 0.1, 0.3, 0.5, 1 and 2 A $g^{-1}$. The corresponding initial discharge capacities are 946.6, 751.7, 592.4, 512.2 and 271.2 mA h $g^{-1}$, respectively. Moreover, when the current density is back to 0.1 A $g^{-1}$, the discharge capacity goes back to 900 mA h $g^{-1}$, which is almost equal to the initial capacity and demonstrates that

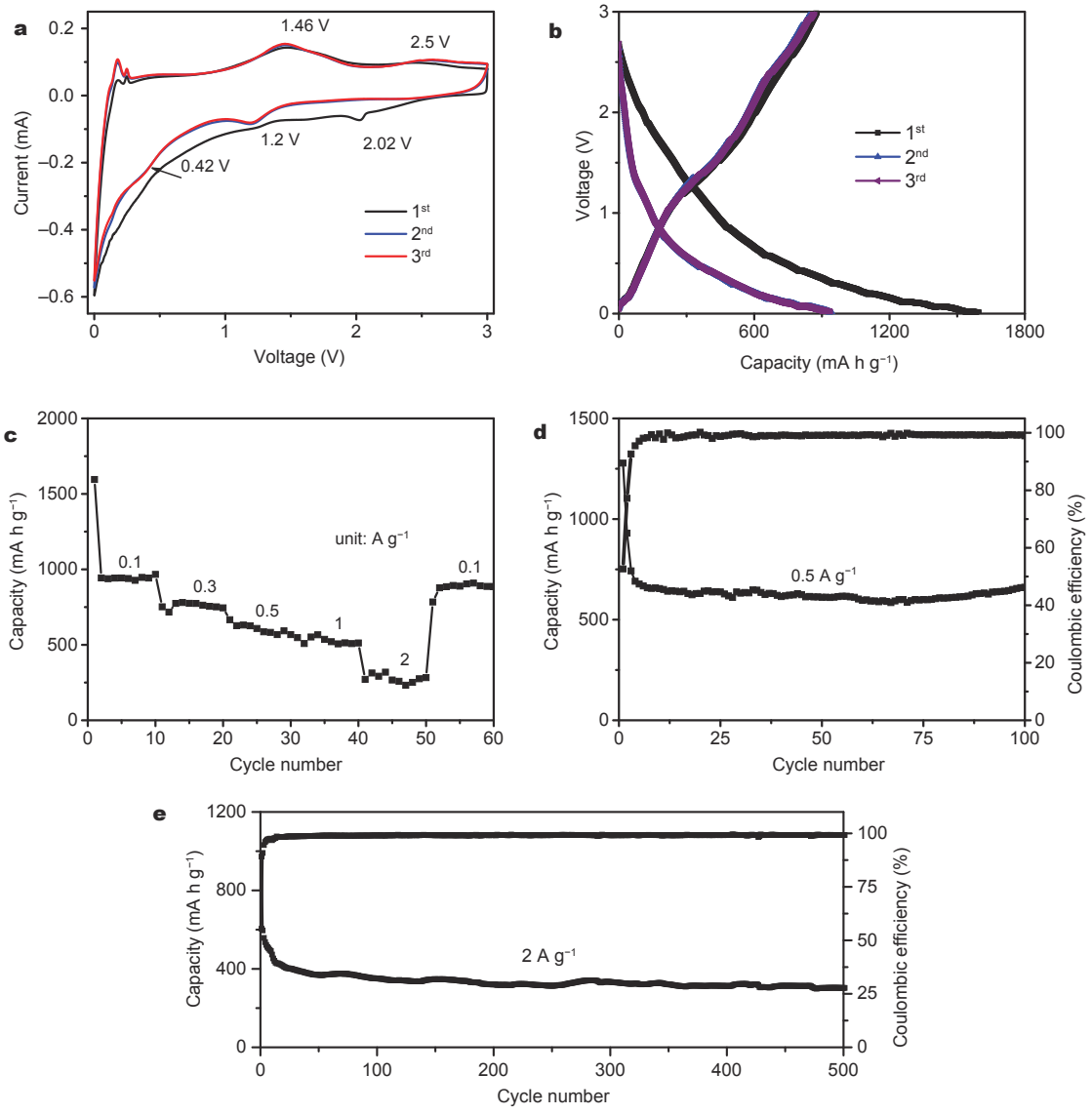


**Figure 5** Electrochemical performances for $Li^+$ storage: (a) CV curves; (b) charge/discharge curves; (c) rate performances of the h-$MoO_3$@C nanofiber electrode; (d, e) cycling performances of h-$MoO_3$@C nanofiber electrode at 0.5 and 2 A $g^{-1}$, respectively.

the h-$MoO_3$@C nanofiber electrode has a good rate performance.

Cycle performance is an important index to evaluate the performance of LIBs. Fig. 5d shows the cycling performances of h-$MoO_3$@C nanofibers at 0.5 A $g^{-1}$. The $MoO_2$@C nanofiber electrode only has 389.9 mA h $g^{-1}$ at the 100$^{th}$ cycle. Compared to $MoO_2$@C nanofiber electrodes, after 100 cycles at the current density of 0.5 A $g^{-1}$, the specific capacity of h-$MoO_3$@C nanofiber electrode still can obtain 660.9 mA h $g^{-1}$. To test the stability of h-$MoO_3$@C nanofiber electrode, the current density of 2 A $g^{-1}$ is carried out, as shown in Fig. 5e. After 500 cycles, the electrodes still can maintain 302.9 mA h $g^{-1}$, remaining structure of the nanofiber from SEM images after cycling in Fig. S4. The properties are not higher than most of publication about $MoO_3$/C for LIBs. A possible reason may be that the $MoO_3$ ratio in the composites is relatively low due to the limitations of electrospinning [56]. On the other hand, the main objective of this study is to *in-situ* transfer $MoO_2$ to h-$MoO_3$, resulting in the synthesis of h-$MoO_3$@C nanofiber with improved electrochemical performance. So it is necessary to calculate the theoretical capacity of the composites, judging the quality of the electrochemical performance. The theoretical capacity of

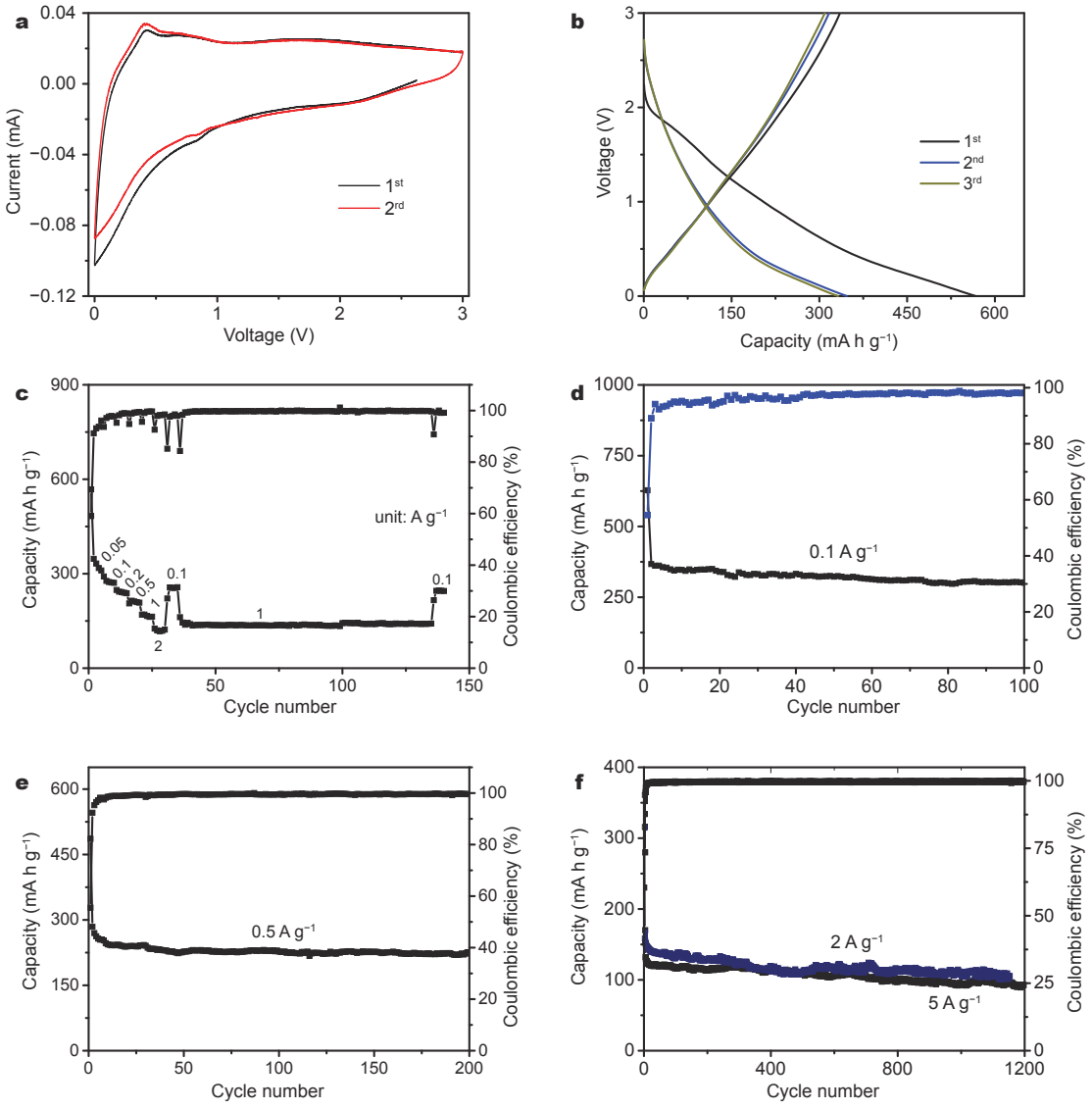


**Figure 6** Electrochemical performances for $Na^+$ storage. (a) CVs; (b) charge/discharge curves; (c) rate performance of the h-$MoO_3$@C nanofiber electrode; cycling performance of $MoO_2$@C (d), h-$MoO_3$@C (e, f) nanofiber electrode at 0.1, 0.5, 1, 2 and 5 A $g^{-1}$, respectively.

h-$MoO_3$@C nanofiber is 567 mA h $g^{-1}$, which is calculated in the Supporting information. With the result, the capacities at 0.1 A $g^{-1}$, even at 0.5 A $g^{-1}$ are higher than the theoretical capacity of h-$MoO_3$@C nanofiber hybrid. Certainly, the electrochemical performances of $MoO_2$@C nanofiber and pure $MoO_3$ at 0.5 A $g^{-1}$ are provided in Figs S5, S6, respectively, which are both lower than that of the h-$MoO_3$@C nanofibers. There are several reasons for the reversible capacity. One is the reversible formation of $Li_2O$ and Mo at nanoscale, according to the following reaction: $MoO_3 + 6Li^+ + 6e^- \leftrightarrow 3Li_2O + Mo$. It has been proved that the small size effect of Mo nanoparticles can greatly increase the electrochemical reactivity and make the conversion between $Li^+$ and $Li_2O$ reversible [57–58]. So nano-Mo metal can probably make extra $Li_2O$ reversibly convert to $Li^+$. Another is the porous nanofiber structure, providing enough active sites for $Li^+$. So it is possible that the specific capacity was higher than theoretical capacity.

It is interesting that the $Na^+$ storage performance of the porous h-$MoO_3$@C nanofiber electrode is also excellent, especially the stability. Fig. 6a shows the CVs of the h-$MoO_3$@C nanofiber electrode at a scan rate of 0.1 mV $s^{-1}$ from 0 to 3.0 V. The oxidation/reduction peaks are 0.4/0 V, associating with the reaction of carbon. The peak

of $MoO_3$ reaction is not obvious. The similar phenomenon is also reported [42,59].

The galvanostatic voltage profile of the h-$MoO_3$@C nanofiber electrode was investigated at current density of 0.05 A $g^{-1}$ over the voltage range of 0–3 V. As shown in Fig. 6b, the initial discharge and charge specific capacity of h-$MoO_3$@C electrodes is 567.2/335.2 mA h $g^{-1}$, respectively. The large capacity losses are attributed mainly to the excessive surface reactions on the SEI films [60].

The rate performances of the h-$MoO_3$@C nanofiber electrodes at 0.05, 0.1, 0.2, 0.5, 1, and 2 A $g^{-1}$ are shown in Fig. 6c. They deliver initial reversible capacity of 567.6, 291.2, 248.4, 205.7, 169.9 and 125.7 mA h $g^{-1}$, still remaining at 141.5 mA h $g^{-1}$ after 100 cycles at 1 A $g^{-1}$. This result proves that the h-$MoO_3$@C nanofiber electrode shows a good rate capability. To study the stability of the h-$MoO_3$@C nanofiber electrode, the cycling performances were tested. In Fig. 6d, after 100 cycles, the $MoO_2$@C nanofiber electrode shows poor stability and capacity retention at the current density of 0.1 A $g^{-1}$. Compared to the $MoO_2$@C nanofibers, the porous h-$MoO_3$@C nanofibers structures not only provide free space for volume expansion, but also facilitate the migration of $Na^+$. As expected, the h-$MoO_3$@C nanofiber electrode can maintain 300.9 mA h $g^{-1}$ at the current density of 0.1 A $g^{-1}$ after 100 cycles, when increased to 0.5, 1 and 2 A $g^{-1}$, respectively, the capacities can still hold 223.1, 153.8 and 108.9 mA h $g^{-1}$ at the $200^{th}$, $500^{th}$ and $1000^{th}$ cycle, respectively (Fig. 6e, f). After pre-cycling at 0.1 A $g^{-1}$, the higher current density (5 A $g^{-1}$) is carried out in Fig. 6f, showing excellent stability with 91 mA h $g^{-1}$ at $1200^{th}$ cycle. The electrochemical performances of $MoO_2$@C nanofibers and pure $MoO_3$ at 0.1 A $g^{-1}$ are also provided in Figs S7, S8, showing the unsatisfactory stability and performances. On the contrary, the porous h-$MoO_3$@C nanofiber can obtain better stability, even higher than relevant publication of $MoO_3$ for SIBs [42,57,61], the reasons for the performance of the porous h-$MoO_3$@C nanofiber electrode for SIBs are summarized as follow: the rich porous structures could not only provide more electrochemical active sites and boost the lithiation/delithiation kinetics, but also facilitate the migration of $Na^+$; the oxygen-containing functional groups on surface form stable chemically bonded SEI films, further enhancing the cyclic stability [47].

## CONCLUSION

In summary, we synthesized porous h-$MoO_3$@C nanofibers by nitric acid oxidizing $MoO_2$@C for LIBs and SIBs. The carbon shell can not only maintain the stability of the structure, but also enhance the conductivity. Moreover, the core shell porous structures provide a large specific surface area of 400.2 $m^2$ $g^{-1}$, which further facilitates structural stability. As the anode materials for $Li^+$/$Na^+$ storage, the porous h-$MoO_3$@C nanofiber electrodes exhibit excellent rate and cycle performances. Therefore, we developed the nitric acid oxidation method to synthesize porous h-$MoO_3$@C nanofibers, which were of improved properties as compared to $MoO_2$@C both in LIBs and SIBs.

**Received 12 June 2017; accepted 11 July 2017; published online 7 August 2017**


1 Mondal AK, Su D, Chen S, *et al.* Mesoporous $MnCo_2O_4$ with a flake-like structure as advanced electrode materials for lithium-ion batteries and supercapacitors. Chem Eur J, 2015, 21: 1526–1532
2 Chakraborty J, Please CP, Goriely A, *et al.* Influence of constraints on axial growth reduction of cylindrical Li-ion battery electrode particles. J Power Sources, 2015, 279: 746–758
3 Raccichini R, Varzi A, Passerini S, *et al.* The role of graphene for electrochemical energy storage. Nat Mater, 2014, 14: 271–279
4 Liu C, Koyyalamudi BB, Li L, *et al.* Improved capacitive energy storage *via* surface functionalization of activated carbon as cathodes for lithium ion capacitors. Carbon, 2016, 109: 163–172
5 Lu J, Chen Z, Ma Z, *et al.* The role of nanotechnology in the development of battery materials for electric vehicles. Nat Nanotech, 2016, 11: 1031–1038
6 Farmann A, Waag W, Marongiu A, *et al.* Critical review of on-board capacity estimation techniques for lithium-ion batteries in electric and hybrid electric vehicles. J Power Sources, 2015, 281: 114–130
7 Wang HG, Yuan S, Ma DL, *et al.* Electrospun materials for lithium and sodium rechargeable batteries: from structure evolution to electrochemical performance. Energ Environ Sci, 2015, 8: 1660–1681
8 Gao G, Lu S, Dong B, *et al.* Mesoporous $Co_3V_2O_8$ nanoparticles grown on reduced graphene oxide as a high-rate and long-life anode material for lithium-ion batteries. J Mater Chem A, 2016, 4: 6264–6270
9 Sun P, Zhao X, Chen R, *et al.* $Li_3V_2(PO_4)_3$ encapsulated flexible free-standing nanofabric cathodes for fast charging and long life-cycle lithium-ion batteries. Nanoscale, 2016, 8: 7408–7415
10 Luo W, Shen F, Bommier C, *et al.* Na-ion battery anodes: materials and electrochemistry. Acc Chem Res, 2016, 49: 231–240
11 Liu Y, Wang X, Song X, *et al.* Interlayer expanded $MoS_2$ enabled by edge effect of graphene nanoribbons for high performance lithium and sodium ion batteries. Carbon, 2016, 109: 461–471
12 Li X, Jiang J, Wang LY, *et al.* A capacity model based on charging process for state of health estimation of lithium ion batteries. Appl Energ, 2016, 177: 537–543
13 Tian L, Zhuang Q, Li J, *et al.* The production of self-assembled $Fe_2O_3$–graphene hybrid materials by a hydrothermal process for improved Li-cycling. Electrochim Acta, 2012, 65: 153–158
14 Chen J, Zhang Y, Zou G, *et al.* Size-tunable olive-like anatase $TiO_2$ coated with carbon as superior anode for sodium-ion batteries. Small, 2016, 12: 5554–5563

15 Hasa I, Dou X, Buchholz D, *et al.* A sodium-ion battery exploiting layered oxide cathode, graphite anode and glyme-based electrolyte. J Power Sources, 2016, 310: 26–31
16 Amani M, Taheri P, Addou R, *et al.* Recombination kinetics and effects of superacid treatment in sulfur- and selenium-based transition metal dichalcogenides. Nano Lett, 2016, 16: 2786–2791
17 He XP, Tian H. Photoluminescence architectures for disease diagnosis: from graphene to thin-layer transition metal dichalcogenides and oxides. Small, 2016, 12: 144–160
18 Akande AA, Rammutla KE, Moyo T, *et al.* Magnetism variations and susceptibility hysteresis at the metal-insulator phase transition temperature of $VO_2$ in a composite film containing vanadium and tungsten oxides. J Magn Magn Mater, 2015, 375: 1–9
19 Kan M, Wang B, Lee YH, *et al.* A density functional theory study of the tunable structure, magnetism and metal-insulator phase transition in $VS_2$ monolayers induced by in-plane biaxial strain. Nano Res, 2015, 8: 1348–1356
20 Hong WT, Risch M, Stoerzinger KA, *et al.* Toward the rational design of non-precious transition metal oxides for oxygen electrocatalysis. Energ Environ Sci, 2015, 8: 1404–1427
21 Shi H, Wang X, Zheng M, *et al.* Hot-electrons mediated efficient visible-light photocatalysis of hierarchical black Au-$TiO_2$ nanorod arrays on flexible substrate. Adv Mater Interfaces, 2016, 3: 1600588
22 Rasmussen FA, Thygesen KS. Computational 2D materials database: electronic structure of transition-metal dichalcogenides and oxides. J Phys Chem C, 2015, 119: 13169–13183
23 Schmidt H, Giustiniano F, Eda G. Electronic transport properties of transition metal dichalcogenide field-effect devices: surface and interface effects. Chem Soc Rev, 2015, 44: 7715–7736
24 Ding Y, Mu D, Wu B, *et al.* Recent progresses on nickel-rich layered oxide positive electrode materials used in lithium-ion batteries for electric vehicles. Appl Energ, 2017, 195: 586–599
25 Majhi K, Bertoluzzi L, Rietwyk KJ, *et al.* Combinatorial investigation and modelling of $MoO_3$ hole-selective contact in $TiO_2$|$Co_3O_4$|$MoO_3$ all-oxide solar cells. Adv Mater Interfaces, 2016, 3: 1500405
26 Yang T, Chen Z, Zhang H, *et al.* Multifunctional $Cr_2O_3$ quantum nanodots to improve the lithium-ion storage performance of free-standing carbon nanofiber networks. Electrochim Acta, 2016, 217: 55–61
27 Massé RC, Uchaker E, Cao G. Beyond Li-ion: electrode materials for sodium- and magnesium-ion batteries. Sci China Mater, 2015, 58: 715–766
28 Wang H, Zhang X. Designing multi-shelled metal oxides: towards high energy-density lithium-ion batteries. Sci China Mater, 2016, 59: 521–522
29 Wang C, Wu L, Wang H, *et al.* Fabrication and shell optimization of synergistic $TiO_2$-$MoO_3$ core-shell nanowire array anode for high energy and power density lithium-ion batteries. Adv Funct Mater, 2015, 25: 3524–3533
30 Opra DP, Gnedenkov SV, Sokolov AA, *et al.* α-$MoO_3$ nanostructure synthesized in plasma by an original method of pulsed high-voltage discharge as highly reversible anode for secondary lithium-ion battery. SSP, 2015, 245: 172–177
31 Yang QD, Xue HT, Xia-Yang HT, *et al.* Low temperature sonochemical synthesis of morphology variable $MoO_3$ nanostructures for performance enhanced lithium ion battery applications. Electrochim Acta, 2015, 185: 83–89
32 Li W, Cheng F, Tao Z, *et al.* Vapor-transportation preparation and reversible lithium intercalation/deintercalation of α-$MoO_3$ microrods. J Phys Chem B, 2006, 110: 119–124
33 Tang Q, Wang L, Zhu K, *et al.* Synthesis and electrochemical properties of H-$MoO_3$/graphene composite. Mater Lett, 2013, 100: 127–129
34 Song J, Ni X, Gao L, *et al.* Synthesis of metastable h-$MoO_3$ by simple chemical precipitation. Mater Chem Phys, 2007, 102: 245–248
35 Chithambararaj A, Sanjini NS, Velmathi S, *et al.* Preparation of h-$MoO_3$ and α-$MoO_3$ nanocrystals: comparative study on photocatalytic degradation of methylene blue under visible light irradiation. Phys Chem Chem Phys, 2013, 15: 14761–14769
36 Chithambararaj A, Rajeswari Yogamalar N, Bose AC. Hydrothermally synthesized h-$MoO_3$ and α-$MoO_3$ nanocrystals: new findings on crystal-structure-dependent charge transport. Cryst Growth Des, 2016, 16: 1984–1995
37 Wang Q, Wang Q, Zhang DA, *et al.* Core-shell α-$Fe_2O_3$@α-$MoO_3$ nanorods as lithium-ion battery anodes with extremely high capacity and cyclability. Chem Asian J, 2014, 9: 3299–3306
38 Zhou W, Xiao X, Cai M, *et al.* Polydopamine-coated, nitrogen-doped, hollow carbon–sulfur double-layered core–shell structure for improving lithium–sulfur batteries. Nano Lett, 2014, 14: 5250–5256
39 Wu J, Qin X, Miao C, *et al.* A honeycomb-cobweb inspired hierarchical core–shell structure design for electrospun silicon/carbon fibers as lithium-ion battery anodes. Carbon, 2016, 98: 582–591
40 Yang Y, Gobeze HB, D'Souza F, *et al.* Plasmonic enhancement of biosolar cells employing light harvesting complex II incorporated with core-shell metal@$TiO_2$ nanoparticles. Adv Mater Interfaces, 2016, 3: 1600371
41 Xia Q, Zhao H, Du Z, *et al.* Synthesis and electrochemical properties of $MoO_3$/C composite as anode material for lithium-ion batteries. J Power Sources, 2013, 226: 107–111
42 Zhang X, Fu C, Li J, *et al.* $MoO_3$/reduced graphene oxide composites as anode material for sodium ion batteries. Ceramics Int, 2017, 43: 3769–3773
43 Chen X, Xiao Z, Ning X, *et al.* Sulfur-impregnated, sandwich-type, hybrid carbon nanosheets with hierarchical porous structure for high-performance lithium-sulfur batteries. Adv Energ Mater, 2014, 4: 1301988
44 Xu G, Han J, Ding B, *et al.* Biomass-derived porous carbon materials with sulfur and nitrogen dual-doping for energy storage. Green Chem, 2015, 17: 1668–1674
45 Wang Q, Yan J, Wang Y, *et al.* Three-dimensional flower-like and hierarchical porous carbon materials as high-rate performance electrodes for supercapacitors. Carbon, 2014, 67: 119–127
46 Chen Z, Yang T, Shi H, *et al.* Single nozzle electrospinning synthesized $MoO_2$@C core shell nanofibers with high capacity and long-term stability for lithium-ion storage. Adv Mater Interfaces, 2017, 4: 1600816
47 Chen Z, Wang T, Zhang M, *et al.* A phase-separation route to synthesize porous CNTs with excellent stability for $Na^+$ storage. Small, 2017, 13: 1604045
48 Shen Z, Hu Y, Chen Y, *et al.* Excimer ultraviolet-irradiated carbon nanofibers as advanced anodes for long cycle life lithium-ion batteries. Small, 2016, 12: 5269–5275
49 Kumar H, Detsi E, Abraham DP, *et al.* Fundamental mechanisms of solvent decomposition involved in solid-electrolyte interphase formation in sodium ion batteries. Chem Mater, 2016, 28: 8930–8941
50 An SJ, Li J, Daniel C, *et al.* The state of understanding of the

lithium-ion-battery graphite solid electrolyte interphase (SEI) and its relationship to formation cycling. Carbon, 2016, 105: 52–76
51 Ji L, Gu M, Shao Y, *et al.* Controlling SEI formation on SnSb-porous carbon nanofibers for improved Na ion storage. Adv Mater, 2014, 26: 2901–2908
52 Li X, Xu J, Mei L, *et al.* Electrospinning of crystalline $MoO_3$@C nanofibers for high-rate lithium storage. J Mater Chem A, 2015, 3: 3257–3260
53 Lu PJ, Lei M, Liu J. Graphene nanosheets encapsulated α-$MoO_3$ nanoribbons with ultrahigh lithium ion storage properties. CrystEngComm, 2014, 16: 6745–6755
54 Lu H, Wu L, Xiao L, *et al.* Investigation of the effect of fluoroethylene carbonate additive on electrochemical performance of Sb-based anode for sodium-ion batteries. Electrochim Acta, 2016, 190: 402–408
55 Ye J, Zang J, Tian Z, *et al.* Sulfur and nitrogen co-doped hollow carbon spheres for sodium-ion batteries with superior cyclic and rate performance. J Mater Chem A, 2016, 4: 13223–13227
56 Zhang M, Yan F, Tang X, *et al.* Flexible CoO–graphene–carbon nanofiber mats as binder-free anodes for lithium-ion batteries with superior rate capacity and cyclic stability. J Mater Chem A, 2014, 2: 5890–5897
57 Xue XY, Chen ZH, Xing LL, *et al.* $SnO_2$/α-$MoO_3$ core-shell nanobelts and their extraordinarily high reversible capacity as lithium-ion battery anodes. Chem Commun, 2011, 47: 5205
58 Bhaskar A, Deepa M, Narasinga Rao T. $MoO_2$/multiwalled carbon nanotubes (MWCNT) hybrid for use as a Li-ion battery anode. ACS Appl Mater Interfaces, 2013, 5: 2555–2566
59 Hariharan S, Saravanan K, Balaya P. α-$MoO_3$: a high performance anode material for sodium-ion batteries. Electrochem Commun, 2013, 31: 5–9
60 Zheng T, Xue JS, Dahn JR. Lithium insertion in hydrogen-containing carbonaceous materials. Chem Mater, 1996, 8: 389–393
61 Li Y, Wang D, An Q, *et al.* Flexible electrode for long-life rechargeable sodium-ion batteries: effect of oxygen vacancy in $MoO_{3-x}$. J Mater Chem A, 2016, 4: 5402–5405

**Acknowledgements** The present work was supported by the National Natural Science Foundation of China (51404103, 51574117 and 61376073), Hunan University Fund for Multidisciplinary Developing (2015JCA04), the Fundamental Research Funds for the Central Universities and the Postdoctoral Science Foundation of China (2017M610495).

**Author contributions** Chen Z and Zhang M designed the project. Chen Z performed the main experiments. Liu Y participated in the article work. Zhang H, Ding S and Wang T helped with the experiments and analyzed the data. Chen Z and Zhang M wrote the manuscript, and all the authors revised the manuscript.

**Conflict of interset** The authors declare that they have no conflict of interest.

**Supplementary information** Supporting data are available in the online version of this paper.

**Zhi Chen** is a PhD candidate at the School of Physics and Electronics, Hunan University. His current research is focused on transition metal oxides and porous carbon for energy storage and conversion.

**Yongkang Liu** is a graduate student at the School of Physics and Electronics, Hunan University. His current research is focused on nano-catalyst.

**Ming Zhang** is an associated professor in Hunan University since 2012. His research is focused on the design and synthesis of nanocomposites for supercapacitors, lithium ion batteries, and gas sensors. He has published more than 50 papers with more than 2600 citations.

## 原位液相转变制备多孔h-$MoO_3$@C纳米线用于锂/钠离子储存

陈智[1†], 刘永康[1†], 张航[2], 丁双双[1], 王太宏[1], 张明[1*]

**摘要** 基于金属氧化物存储机制, $MoO_3$比$MoO_2$具有更高的理论容量. 本文通过热的硝酸氧化$MoO_2$@C纳米线成功制备出具有400.2 $m^2\ g^{-1}$高比表面积的多孔h-$MoO_3$@C纳米纤维, 且碳壁没有明显破坏. 作为锂离子电池的负极, 与$MoO_2$@C纳米线相比多孔h-$MoO_3$@C纳米纤维电极表现出更好的性能, 其中在2 A $g^{-1}$的电流密度下500循环后展现出302.9 mA h $g^{-1}$的可逆容量. 作为钠离子电池的负极, h-$MoO_3$@C电极同样具有很好的倍率性能. 在2 A $g^{-1}$的电流密度下500循环后仍具有108.9 mA h $g^{-1}$的容量, 并且在2 A $g^{-1}$的电流密度下1200循环后还能保持91 mA h $g^{-1}$的容量. 由于碳壁可以维持结构的完整性且可提高导电性; 同时h-$MoO_3$ 的隧道结构可作为分离电子孔并为$Li^+$/$Na^+$ 嵌入脱出提供更多的特有位置, 使得该复合纳米线作为电极材料表现出更好的性能. 本工作为合成具有高价的过渡金属氧化物/碳复合材料在电池和催化剂领域的运用提供了依据.